A Case Study: The Indirect Aerosol Effects of Mineral Dust on Warm Clouds

R. LI, Q.-L. MIN, AND L. C. HARRISON

Atmospheric Science Research Center, University at Albany, State University of New York, Albany, New York

(Manuscript received 18 June 2009, in final form 4 September 2009)

ABSTRACT

The indirect aerosol effect (Twomey effect) is studied during a Saharan dust-transport event that presented an unusually favorable combination of a dust-loading gradient across clouds with warm cloud-top temperatures. Standard retrievals from the Moderate Resolution Imaging Spectroradiometer (MODIS), the Advanced Microwave Scanning Radiometer for Earth Observing System (AMSR-E), and the Clouds and the Earth's Radiant Energy System (CERES) provide cloud-top temperature (a surrogate for height), liquid water path (LWP), classification of precipitation regime, and radiation flux. The authors correlate a retrieved mean effective droplet radius (r_e) versus the number concentration of cloud condensation nuclei (N_{CCN}), using the regressed slope $d\ \ln r_e/d\ \ln N_{CCN}$ as the estimator of the aerosol indirect effect (AIE). Results demonstrate statistically significant AIE for only some of the segregated cloud classes. For nonprecipitating clouds (the most direct test of Twomey effect), the estimated AIE is effectively -0.07 over all wider temperature bands and is statistically significant from 1.1 to 1.9 σ. Further classification by LWP strengthens both the AIE (for all LWP > 150 g m^{-2}) to approximately -0.16, and substantially increases the statistical significance, to better than 5σ.

Shortwave radiation forcing of dust aerosols is also estimated directly from satellite measurements. The direct shortwave (SW) radiation effect of Saharan dusts at solar zenith angle 21.6° is 53.48 ± 8.56 W m^{-2} per unit aerosol optical depth, with a correlation coefficient of 0.92. The indirect SW forcing of Saharan dust is 29.88 ± 2.42 W m^{-2} per unit AOD for clouds with LWP of 100 g m^{-2}.

1. Introduction

An increase in the effective number concentration of cloud condensation nuclei (CCN) is presumed to lead to higher cloud droplet numbers, smaller droplet sizes, and larger optical depth at constant cloud water content, that is, the Twomey effect (Twomey 1977a,b), and to inhibition of drizzle and resultant increase of cloud liquid water and lifetime (Albrecht 1989). There is ample evidence of aerosol indirect effects from in situ and remotely sensed observations during intensive field campaigns (Ackerman and Toon 2000; Ramanathan et al. 2001), satellite surveys (Han et al. 1998; Schwartz et al. 2002), and more recently from ground-based observations (Feingold et al. 2003; Kim et al. 2003). Unfortunately, the attributed magnitudes of the various kinds of indirect radiative forcing are quite uncertain because they involve subtle changes in cloud radiative properties and lifetimes (Rosenfeld and Feingold 2003; Shao and Liu 2005). There are many issues regarding the degree to which these occur, the factors that control these processes, and tests to make inferences independent. Furthermore, most larger-scale statistical studies of the first indirect effect (Twomey effect) have been done without either distinguishing cloud precipitation regimes or excluding the precipitating clouds from the analysis. Clearly precipitation processes can influence the observed microphysics substantially. It is important to understand aerosol impacts on precipitating clouds, particularly residual cloud droplets in the tops of precipitating clouds. Our analysis attempts to discern these competing factors as best we can, given the statistical limits of the data available.

Mineral dust is one of four major aerosol sources in the atmosphere; its composition and CCN properties differ substantially from other aerosols. Saharan dust can be transported across the Atlantic Ocean and influence the intensity of Atlantic hurricanes and cloud systems (Dunion and Velden 2004). Dust transport from

Corresponding author address: Q.-L. Min, Atmospheric Sciences Research Center, CESTM, University at Albany, State University of New York, 251 Fuller Road, Albany, NY 12203.
E-mail: min@asrc.cestm.albany.edu

DOI: 10.1175/2009JAS3235.1

the Gobi to the west coast of the Americas is also often seen (Sassen 2002). Min et al. (2009) found that for a given convection strength there were more small-sized hydrometeors and less large-sized hydrometeors in regions of stratiform rain polluted with dust: a demonstration of the Albrect effect for these aerosols.

Perhaps the principal difficulty in substantiating aerosol effects on clouds and precipitation is that cloud evolution is affected profoundly not only by aerosols and associated microphysical processes but also by cloud dynamics. Without specific constraints on cloud conditions it is unclear whether a smaller cloud drop size is due to a higher CCN concentration, less condensed water, or different cloud dynamics (Rosenfeld and Feingold 2003; Schwartz et al. 2002; Twomey 1974). Another general worry about studies of this kind is that—absent statistical controls—there may be hidden correlations between aerosol properties and cloud dynamics from the weather transport processes and sources. Such a ''hidden control variable'' could cause attribution of aerosol effects that were not really the result of cloud microphysics.

Olson et al. (2001) show that the horizontal variability of the observed brightness temperatures at 19 and 37 GHz (both horizontal polarization) and rainfall intensity provides a diagnostic of cloud convective intensity. We use this measure and also cloud-top temperature (CTT) and cloud liquid water path (LWP) to segregate clouds into population classes with more uniform cloud dynamics. By doing this we achieve much stronger statistical significance for the warm-cloud AIE, even though the population of each class is reduced considerably. We calculate the impact of spatial correlation on the degrees of freedom used to calculate these statistical uncertainties; this reduces our stated statistical significances compared to studies that have assumed all observations are independent. We assess the direct and indirect radiation forcing produced by the mineral dust of this event from these data and satellite observations of upwelling shortwave flux.

2. Case selection and data description

In this study we analyze a remarkable single case of Saharan dust transport over the Atlantic, which occurred in March 2004, shown in Fig. 1. Data are from combined retrieval products of the Moderate Resolution Imaging Spectroradiometer (MODIS), Clouds and the Earth's Radiant Energy System (CERES), and the Advanced Microwave Scanning Radiometer for Earth Observing System (AMSR-E) instrument systems: data extend from 5°S to 4°N, 10°W to 5°E.

We chose this case based on several requirements: 1) a large variation in dust concentration within a cloud system; 2) the statistics of cloud-top temperature and classification into precipitating and nonprecipitating clouds are nearly independent of the dust loading; 3) most of those clouds have cloud-top temperatures above −20°C and there are large populations of cloud-top temperatures at 0°C and above; and 4) a set of satellite sensors on radiation, aerosol, clouds, and precipitation are available at the time. Cases that satisfy all these requirements are rare, particularly those demonstrating large populations of warm cloud tops (necessary for direct tests of the Twomey effect). This Saharan dust event in March 2004 was one of the greatest dust outbreaks since 2002 (when all the satellite data used here became available) and the only event from 2002 to 2008 that met all these criteria. Also, we are very fortunate that surface-based in situ measurements of the dust size distribution and chemical composition were collected aboard the NOAA ship *Ronald H. Brown* during the Trans-Atlantic Saharan Dust Aerosol and Ocean Science Expedition (AEROSE) campaign (Nalli et al. 2005, 2006; Morris et al. 2006).

This event was identified as a dust event by the MODIS Rapid Response Project (see http://rapidfire.sci.gsfc.nasa.gov/gallery/?2004067-0307/Dust.A2004067.1350.8km.jpg; MODIS observation) and the NOAA Operational Significant Event Imagery (OSEI) team (see http://www.osei.noaa.gov/Events/Dust/Africa_W/2004/DSTafr067_G12.jpg; GOSE observation) as described in Nalli et al. (2006): ''The *Ronald H. Brown* entered the dust event on the following day, 7 March 2004, ... Dust settled onto the ship in a dense haze similar to that described by Carlson and Prospero (1972).'' The *Terra* and *Aqua*/MODIS retrieved aerosol optical depth (AOD) in large (coarse) and small (fine) modes at 550 nm on 7 March 2004 show that the coarse-mode AOD ranged from 1.5 to 4.0, much larger than the fine mode AOD. All data demonstrate that mineral dust dominates this case. No fires in the upwind region were detected by either the MODIS Rapid Response Team or the OSEI scene classifications.

The MODIS standard product MYD06 is used to obtain cloud liquid water path, cloud optical depth, cloud phase, and cloud-top temperature. These data are at 5-km resolution. We collocated the MODIS retrievals with AMSR-E rainfall products. The AMSR-E/*Aqua* L2B global swath rain rate and rain type are retrieved using the Goddard profiling algorithm, which was originally developed in 1996 and has undergone significant improvements since Kummerow et al. (2001). A detailed description can be found in Wilheit et al. (2003) and Olson et al. (2006), and references therein. From these we divided MODIS retrievals into three categories: nonraining clouds with AMSR-E retrieved rain rate zero; strong convective raining clouds with AMSR-E

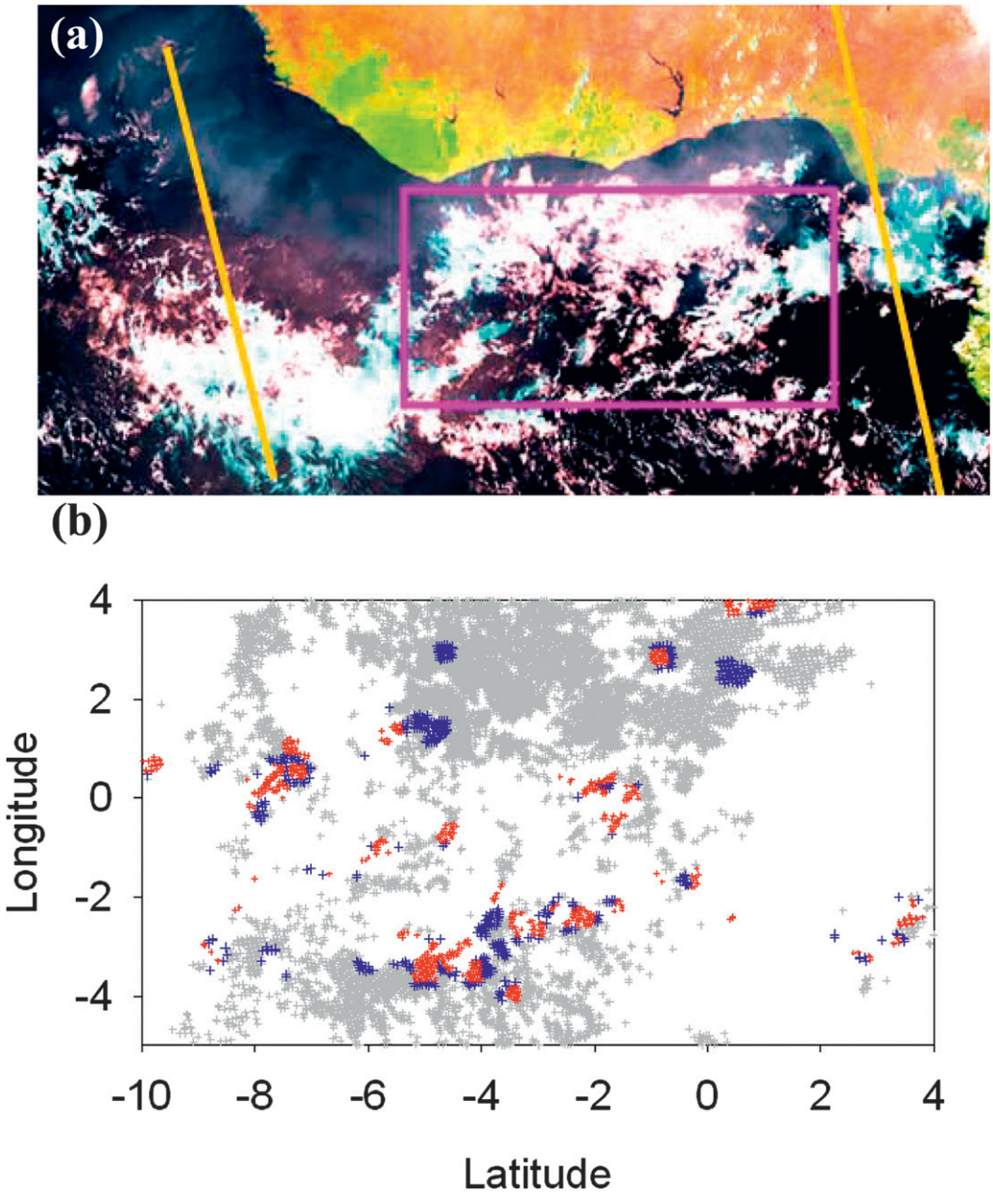

FIG. 1. (a) Clouds (white and blue) and dust plume distribution as seen from the *Meteosat-8* RGB composite on 1345 UTC 7 Mar 2004. (b) The quasi-simultaneous observation of clouds derived from the AMSR-E. Clouds are categorized into groups of strong convective rainy clouds (red), weak convective rainy clouds (blue), and nonraining clouds. Orange lines indicate the swath of AMSR-E. The pink box indicates the selected study area.

retrieved rain rate larger than zero and convective fraction larger than 70%; and weak convective raining clouds with AMSR-E retrieved rain rate larger than zero and convective fraction less than 70%. The threshold of 70% is not critical to the results, as shown by sensitivity tests in which this threshold was shifted to 60% or 80%. We also combined CERES radiation measurements from the Single Scanner Footprint (SSF) products with cloud properties from MODIS within the common footprint of 20 km (Geier et al. 2003).

Inspection of *Meteosat-8* images shows that the MODIS dust/cloud screen appears to have failed in the northwest corner where the dust loadings are very high, and dust is misidentified as nonraining clouds. We removed the data west of −8° longitude and north of 2° latitude. This affects only clouds identified as nonraining, a small portion of

those data. However, we will show later this did not eliminate all cloud/dust screening errors, and there are some other results which appear aphysical or at least unlikely. Extensive uncertainty analysis has been done by the MODIS team; they estimated that the uncertainty in the MODIS effective radius retrieval is generally less than 1 μm (King et al. 1997). Also, as summarized in Kaufman et al. (2005), retrievals are not affected by overlying aerosol, and the cloud optical depth retrievals have small errors due to aerosol contamination.

The cloud phase classification in MODIS provides four categories: water, ice, mixed, and ''uncertain.'' The separation of ice and water is based on the fact that the imaginary index of refraction for water and ice are distinct from 10–13 μm but similar at 8.5–10 μm. So far there is no published evidence of large bias in MODIS cloud phase classification. In our study, we excluded those samples of ice, mixing, and uncertain phase. The identified water clouds with cloud-top temperature colder than 0°C are ~38% of the total valid samples.

Current passive microwave algorithms may introduce uncertainties in rain/nonrain classification at large LWP (>300 g m^{-2}, Berg et al. 2006). However, in our study, this will not affect our results severely because the nonraining sample with large LWP (>300 g m^{-2}) is only 1.09% of the total sample.

Additionally, the stability and absolute accuracy of CERES measurements are estimated to be 0.2% and 0.5%, respectively (Wielicki et al. 1996).

All studies of this kind are hampered by the obvious retrieval problem: we can retrieve aerosol information only outside the clouds. In this cloud system the dust is advected southward. We used the cloud-mask data to discriminate against cloud pixels and then constructed a one-dimensional north–south profile, which amounts to zonally averaged column CCN concentrations and aerosol optical depths, as retrieved by MODIS. Column CCN concentration and AOD decreased monotonically from 4°N to 1°S and were almost constant farther south (Fig. 2).

Satellite estimation of CCN concentration from optical backscatter is a difficult problem, and the MODIS CCN algorithm has been criticized (Gassó and Hegg 2003; Kapustin et al. 2006). In this case the MODIS CCN product and AOD are so strongly correlated that they are effectively surrogates for each other (Fig. 2). This is expected in a scene in which the aerosol type classification needed by the MODIS CCN product remains invariant (dust in this case, of course). We have tested our AIE regressions using either the CCN product or AOD against each other: in this case the results are statistically indistinguishable.

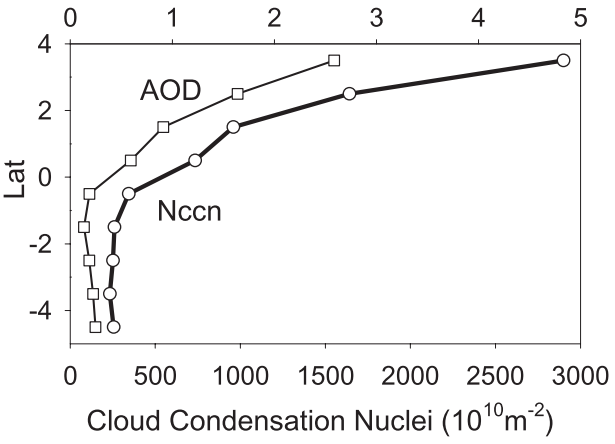

FIG. 2. The zonal mean profiles of the aerosol optical depth and the number of cloud condensation nuclei (N_{CNN}) retrieved from *Aqua* MODIS observation in the study area.

3. Methodology

There are at least four key factors that influence cloud droplet effective radius directly: cloud updraft velocity, cloud temperature, cloud liquid water path, and CCN concentration. Direct measurements of updraft velocity at cloud base from satellite measurements are not available. As mentioned, the convective fraction can be regarded as a surrogate for the updraft strength of tropical convective clouds (Olson et al. 2006). Nonraining clouds generally have the weakest convective intensity. Clouds classified as strong convective raining exhibit the strongest updraft and an inhomogeneous rainfall rate. The weak convective raining clouds have mild updraft and a relatively homogenous rainfall rate (Houze 1997).

Cloud-top height is an additional constraint on cloud convection. We further segregated our observations into five cloud-top height categories according to the cloud-top temperature (CTT): −20° to −10°C, −10 to 0°C, 0° to 10°C, 10° to 20°C, and 20° to 30°C. There are very few observations in the 0° to 10°C range; the population distribution is bimodal with a minimum here. The warmest cloud-top temperatures are of course the lowest clouds. In each cloud precipitation regime with the same cloud-top height, we assume that clouds have similar dynamics. Because of the bimodal distribution of cloud-top temperatures, we also produce statistics for the ranges −20° to 4°C and 4° to 20°C, providing aggregated statistics for the two modes seen. For reasons discussed later we do not include data with temperatures above 20°C in the second of these ranges.

Cloud drop size can be modulated not only by CCN concentration (N_{CNN}) but also by condensed cloud water. An important requirement for the Twomey effect is to compare the cloud droplet size for the same LWP.

Few studies of aerosol indirect effects have done this, likely facing the same difficulty as we do. With limited data and resulting concern over statistical significance, we cannot further classify by LWP directly for all cases. Instead, for our primary analysis we calculated r_e = LWP/($\rho_w\tau$), where ρ_w is the density of water (10^6 g m^{-3}) and τ is cloud optical depth, as a surrogate estimator of cloud droplet radius. These two parameters are more directly retrieved from measurements of absorption and nonabsorption channels of MODIS than the inferred cloud effective radius. Since cloud optical depth and cloud LWP are functions of second and third moments of cloud drop size distribution, this ratio is directly linked to the cloud effective radius. For multiple samples, a linear regression between the two parameters provides a better weighted indicator of cloud effective radius than the simply averaged cloud effective radius (Kim et al. 2003). To the extent that LWP and cloud optical depth are properly sensed for the whole column, the r_e derived from their ratio is a reasonable column average. However, due to limited photon penetration into thick clouds, the optically retrieved cloud LWP and optical depths may be underreported for the thickest clouds and relevant only to their upper portions. We believe that this is not a substantial issue for any clouds except the thickest convective clouds.

We then regress lnr_e versus ln$N_{\rm CNN}$, segregated into classes both by cloud type and cloud-top temperature. AIE = d lnr_e/d ln$N_{\rm CNN}$ is a measure of the aerosol indirect effect. These regressions are done as simple linear regressions, assuming that $N_{\rm CNN}$ is more certain than our inferred r_e. This is formally true for the error estimates propagated from the satellite analyses, particularly given that $N_{\rm CNN}$ is computed as a zonal average over pixels. However, this clearly does not capture the real variance of the aerosols around and under these cloud systems, which we cannot observe. We have also done the regressions minimizing the geometric distance (effectively assuming that the uncertainties are equal in both parameters) with no significant change in the regressed slopes.

These spatial data have internal correlation: one cannot assume that each observed pixel represents an independent trial for the purpose of estimating the statistical significance. The analysis of the true degrees of freedom of the data used for each regression is itself a potentially disputatious problem. So far as we know, there is no analytic expression for the number of degrees of freedom contained by sampled data with irregular spacing, even for the simplest case, which assumes an isotropic exponentially decaying correlation versus range. We present the analysis done with four differing assumptions in the appendix, in part to justify a formal assumption made but also to show that the differences are not large. We use the most common assumption for the estimate of the degrees of freedom presented here; the others are listed in the appendix.

These regressions are shown in Fig. 3, and the results are listed in Table 1. For convenience this table also includes one measure of the degrees of freedom (Dfe) of the pixels in the data, as well as resulting estimates of statistical significance. We have the most data for nonraining clouds; we can further stratify these data into four different ranges of LWP: 75–150, 150–225, 225–300, and 300–375 g m^{-2}. Within these LWP bins, the variations of cloud droplet size are generally small. Based on the effective radius retrieved by MODIS, the standard deviations are about 1.5–3.5 against the mean value 11.6–16.6. Since we used r_e = LWP/τ in our study, the width of a LWP bin generates little uncertainty in the calculations of AIE.

The AIE are also computed separately for two aggregated temperature ranges, −20° to 4°C, and 4° to 20°C, shown in Table 2. The latter of these is expected to be the broadest statistical test for the Twomey effect, and gratifyingly it shows large AIE and strong statistical significance.

4. Results

a. *Twomey effect*

In a strict sense, the Twomey effect can be tested (isolated from other effects) only in nonprecipitating clouds. This case is advantageous in having more that 50% nonprecipitating cloud. The regressions of lnr_e versus ln$N_{\rm CNN}$ show statistically significant aerosol indirect effect (a negative coefficient) broadly and in all categories except the temperature range 20° to 30°C, where the coefficient is positive (+0.04) and apparently significant at better than 99% probability! To highlight this element it is shown in bold in Table 1. This anomaly forces a closer look at these data, and it is evident that the cloud-screening algorithm is failing for some pixels with very high dust loadings; these pixels are being mistakenly identified as clouds. The dust is at low altitudes and so contaminates only the data with cloud-top temperatures greater than 20°C. Data with cloud-top temperature above 20°C are excluded from all further results.

Ignoring this contaminated data range, all other nonraining clouds classified only by cloud-top temperature consistently show an AIE with a regressed AIE coefficient of near −0.07 (−0.066, −0.072, and −0.052 for nonraining clouds in the respective range −20° to −10°C, −10° to 0°C, and 10° to 20°C), with statistical significances between 1.1σ and 1.9σ. The range 0°−10°C appears to show a stronger AIE (−0.22), but this domain has little data (it is a minimum in the bimodal distribution of cloud-top temperatures);

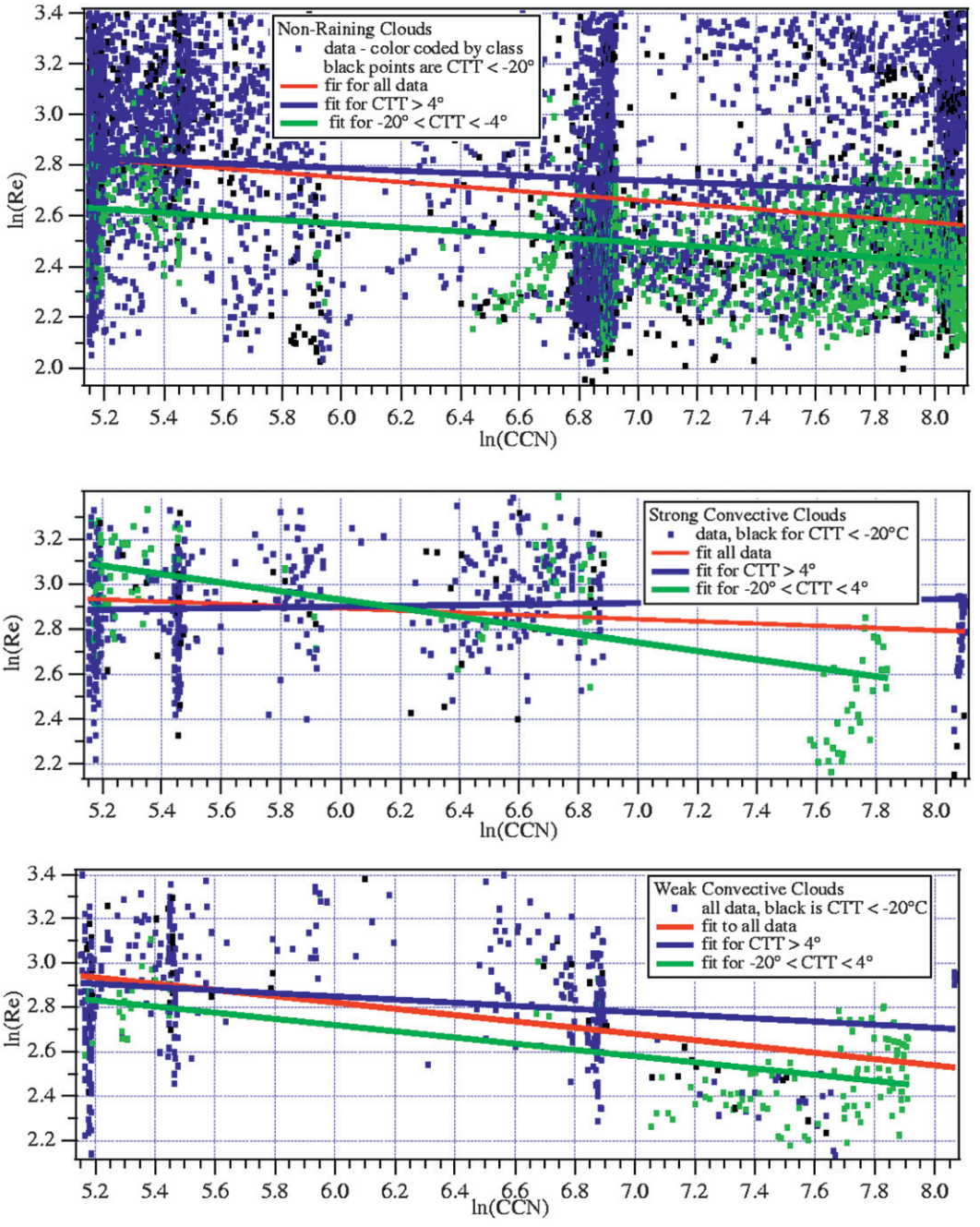

FIG. 3. Scatterplots of $\ln r_e$ against $\ln N_{\mathrm{CNN}}$ for (from top to bottom) strong convective rainy clouds, nonraining clouds, and weak convective rainy clouds. Linear regression are made by using all data, data with cloud top temperature warmer than 4°C, and data with cloud-top temperature 4°~−20°C, respectively.

note also that the standard error [Se(Dfe)] is large (0.12), large enough that the AIE in this temperature range is not, in fact, significantly different from the other temperature ranges. The consistency of these results is encouraging; it abets the analysis by LWP because to do so we would like to use larger cloud-top temperature classifications to preserve degrees of freedom.

Classifying these nonraining cloud data by LWP for the two modes of the cloud-top temperature distribution (Table 2) shows interesting results:

- For the data in the cloud-top temperature range −20° to 4°C and stratified by LWP, we see that the observed AIE appear to show similar AIE (−0.05 to −0.07) for

TABLE 1. Calculations of aerosol indirect effect for all clouds segregated by cloud-top temperature. From left to right: the number of pixels contributing (N), the degrees of freedom estimated as discussed (Dfe), AIE, Pearson's correlation coefficient (R), the expected standard error in AIE if all pixels are independent [Se(N)], the expected standard error in AIE given the estimate of degrees of freedom [Se(Dfe)], and the ratio AIE/Se(Dfe), which is the statistical significance of the regressed AIE, in standard deviations.

CTT (°C)	N	Dfe	AIE	R	Se(N) (10^{-3})	Se(Dfe) (10^{-3})	AIE/Se(Dfe)
Non-raining clouds: All data, segregated only by temperature							
−20∼−10	1044	17.46	−0.066	−0.32	7.06	57.93	−1.142
−10∼0	1091	17.93	−0.072	−0.31	7.37	60.94	−1.175
0∼10	393	9.21	−0.217	−0.58	16.63	122.50	−1.768
10∼20	3053	95.40	−0.052	−0.20	4.82	27.53	−1.906
20∼30	2149	134.66	**0.043**	0.28	3.11	12.52	3.401
−20∼4	2144	30.22	−0.074	−0.34	5.12	44.61	−1.664
4∼20	3437	97.57	−0.066	−0.24	4.73	28.35	−2.325
Strong convective rainy clouds: All data, segregated only by temperature							
−20∼−10	52	6.79	−0.148	−0.46	54.95	177.50	−0.835
−10∼0	73	6.48	−0.184	−0.74	18.52	73.74	−2.500
0∼10	25	4.18	−0.014	−0.04	64.29	208.80	−0.065
10∼20	282	45.91	0.020	0.08	16.10	40.65	0.490
20∼30	180	53.08	−0.002	−0.01	15.49	28.91	−0.086
−20∼4	126	12.56	−0.190	−0.67	18.43	63.16	−3.011
4∼20	306	47.73	0.020	0.08	16.01	41.27	0.491
Weak convective rainy clouds: All data, segregated only by temperature							
−20∼−10	60	5.07	−0.193	−0.75	22.37	97.30	−1.981
−10∼0	66	4.57	−0.109	−0.40	25.44	126.91	−0.856
0∼10	35	3.35	−0.274	−0.73	59.45	294.43	−0.930
10∼20	207	17.46	0.012	0.04	20.32	73.98	0.164
20∼30	147	23.14	0.010	0.04	18.56	48.61	0.208
−20∼4	127	8.39	−0.140	−0.57	16.28	72.00	−1.942
4∼20	241	19.38	−0.054	−0.19	19.50	72.32	−0.748

all LWP categories (except for the thickest LWP bin of 300−375 g m^{-2}), but that the individual statistical significances are weaker, due to loss of degrees of freedom. Only the lowest LWP range achieves an AIE/Se(Dfe) greater than one, and that marginally so (1.2σ). The differences between these AIE for the LWP classes are not statistically significant for the data in this colder cloud-top temperature range. LWP is not diagnostic for these higher/colder cloud tops. Again, the rain/no-rain discrimination of clouds with LWP > 300 g m^{-2} is suspect.

- In contrast, the same LWP segregation applied to the CTT range 4° to 20°C shows the strongest and most statistically significant regressions for the observed AIE = −0.07 to −0.17 in our data, ranging from 2.26σ to 5.47σ. The difference between the AIE for the first two LWP ranges is statistically significant; the observed AIE is weaker for the lowest LWP clouds and not distinctly different for the greater LWP ranges.

In the strong convective raining clouds, only those with the coldest cloud-top temperatures show statistically significant negative correlation (AIE = −0.15 to −0.18), and these are significant to 2.5σ. It is hard to explain how the Twomey effect could give us this result; in precipitating clouds, the effects of precipitation efficiency, and also rain scavenging of input aerosols, appear to dominate.

In the weak convective raining clouds, again, only the clouds with the coldest tops show statistically significant sensitivity of mean effective radius to aerosol loading (−0.19), at 1.9σ. These results are interesting and present something of a puzzle. In these clouds we see that the AIE coefficient and its significance for the CTT range −20° to −10°C is much stronger than that for the −10° to 0°C range (unlike the strong convective-raining cloud behavior). This hints at ice nucleation physics as a mechanism for the observed effect, as the Saharan dust aerosols are known to be good ice nuclei at temperatures below −5 to −8°C (Toon 2003). However, all of the clouds here are classified as warm clouds; all clouds identified as mixed phase are not included in the study. Hence, this hypothesis would require an effect from clouds with too small an ice concentration for the satellite data product to see; no strong explanation presents itself for this observed correlation.

TABLE 2. Calculations of aerosol indirect effect for nonraining clouds segregated by cloud-top temperature and liquid water path; NC = not calculated.

LWP range (g m^{-2})	N	Dfe	AIE	R	Se(N) (10^{-3})	Se(Dfe) (10^{-3})	AIE/Se(Dfe)
			CTT range: −20° to 4°				
70–150	957	17.72	−0.070	−0.35	7.03	54.77	−1.274
150–225	490	12.47	−0.059	−0.31	10.00	68.30	−0.857
225–300	229	8.09	−0.049	−0.27	17.11	104.47	−0.474
300–375	23	1.52	−0.118	−0.80	19.78	NC	NC
			CTT range: 4° to 20°C				
75–150	941	73.22	−0.066	−0.26	8.06	29.27	−2.266
150–225	233	38.69	−0.166	−0.67	12.07	30.28	−5.471
225–300	75	17.78	−0.162	−0.71	13.78	29.64	−5.453
300–375	38	8.00	−0.124	−0.78	12.69	31.12	−3.982

b. Dust-induced direct and indirect shortwave radiation forcing

Saharan dust is a significant direct climate forcing owing to scattering and absorption of solar radiation as well as indirect forcing through impacts on cloud and precipitation characteristics. Accurate assessment of direct and indirect SW radiation forcing of dust is necessary to understand its impacts on cloud systems. Efforts have been made to estimate the direct and indirect radiation forcing by dust, mostly with the aid of radiation transfer models. To assess dust radiation effects directly from measurements, particularly indirect radiation forcing, we use the CERES Single Scattering Footprint data from both FM3 and FM4 operating modes. Given the extreme concentration of Saharan dust in this case, we ignore the contributions of other aerosols including sea spray, smoke, and anthropogenic aerosols.

There are insufficient 100% clear-sky CERES fields of view (FOVs) in the selected area to calculate direct SW forcing. Thus, we define "clear sky" FOVs as those with CERES-observed clear sky fraction larger than 90%. Although the remaining cloud fractions are small, they clearly impact the upwelling SW flux in a nearly linear way, as shown in Fig. 4a. We fit a slope coefficient for the clear-sky fraction and the top-of-atmosphere (TOA) flux (Fig. 4a) and then use this slope to extrapolate the observed SW radiation to 100% clear sky. The longitudinal distribution of such equivalent SW is shown in Fig. 4b. It is clear that the upwelling clear-sky SW increases dramatically with aerosol optical depth, indicating a significant negative SW forcing for the atmosphere. We define the direct SW radiation forcing as the regression slope between the zonal mean SW and the AOD (Fig. 4c). This analysis yields a direct SW radiation forcing by Sahara dust of 53.48 ± 8.56 W m^{-2} per unit AOD at mean solar zenith angle 21.6° (with the range from 15.9° to 28.5°) with a correlation coefficient of 0.92. This result is generally consistent with the estimations of Liu et al. (2003) (~50 W m^{-2} per unit AOD)

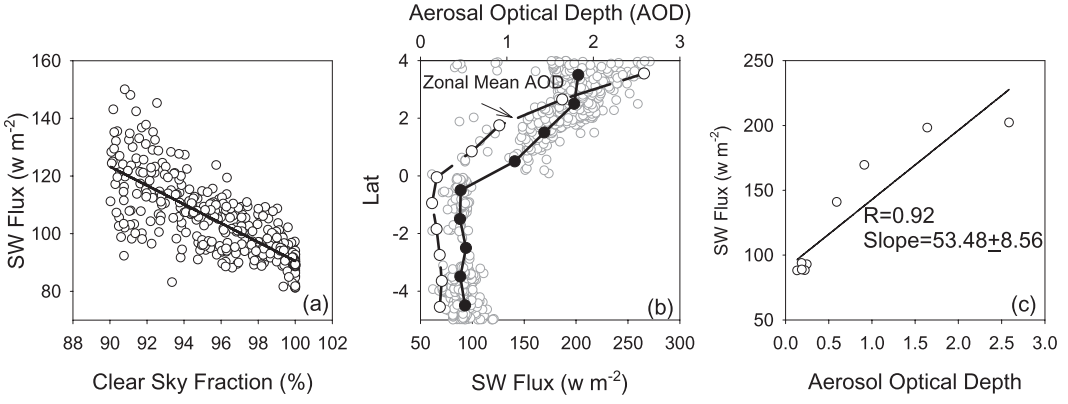

FIG. 4. (a) Correlation between SW flux and the clear-sky fraction in selected "clear sky" FOVs. (b) Latitudinal distribution of 100% clear-sky SW and the zonal mean AOD. (c) Correlation between zonal mean 100% clear-sky SW and AOD.

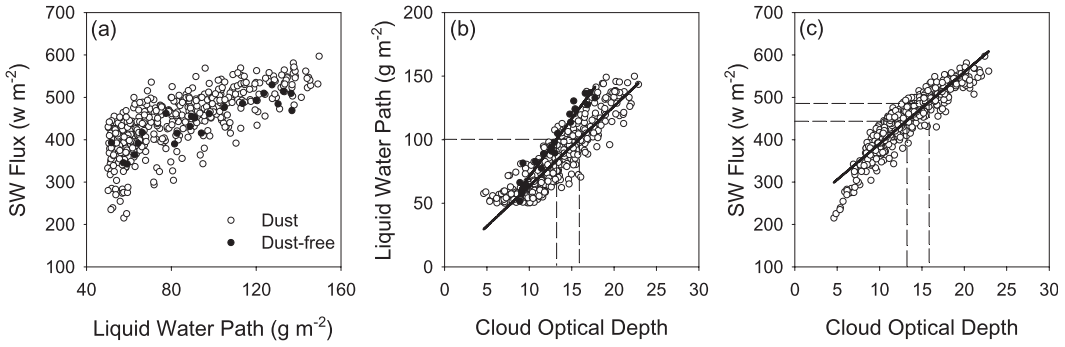

FIG. 5. (a) Correlation between 100% cloudy-sky SW flux and LWP. (b) Correlation between LWP and cloud optical depth. (c) Correlation between 100% cloudy-sky SW flux and cloud optical depth.

and Christopher and Jones (2007) (47.91 ± 3.81 W m^{-2} per unit AOD), although the study area and temporal scale are different in these studies.

As demonstrated, the Twomey effect strongly depends on cloud LWP. To have statistically sufficient samples, we focus on single-layer nonprecipitating clouds in CERES footprints with LWP between 50 and 150 g m^{-2} in both dusty and dust-free regions. The constraint information comes from the CERES SSF product.

Again, there are insufficient 100% cloudy-sky CERES FOVs in the selected area to calculate indirect SW forcing. A FOV is defined as "cloudy sky" when the CERES-observed cloud fraction was larger than 70%. SW radiation coming from such mixed sky FOVs is contributed by both clear sky and cloudy sky and again must be scaled to 100% cloudy-sky SW. To do this, we assume that

$$\mathrm{SW\_mix} = \mathrm{SW\_clr} \times \mathrm{Frc} + \mathrm{SW\_cld} \times (1 - \mathrm{Frc}),$$

$$\mathrm{SW\_cld} = (\mathrm{SW\_mix} - \mathrm{SW\_clr} \times \mathrm{Frc})/(1 - \mathrm{Frc}),$$

where SW_clr, SW_cld, and SW_mix stand for SW flux from 100% clear sky, 100% cloudy sky, and mixed sky; Frc stands for clear-sky fraction.

Correlations between the 100% cloudy-sky SW and LWP are shown in Fig. 5a. The SW increases with LWP; the correlation between LWP and cloud optical depth and the results are shown in Fig. 5b. At a given LWP of 100 g m^{-2}, the associated cloud optical depth is larger in the dust sector (15.81 ± 0.67) than in the dust-free sector (13.18 ± 1.33)—evidence of Twomey effect. We use these values to calculate the associated SW indirect radiation forcing based on Fig. 5c. The associated 100% cloud sky SWs are 488.68 ± 11.51 (2.4%) W m^{-2} and 444.16 ± 22.52 (5.7%) W m^{-2} in dust and dust-free sectors, respectively. The associated AOD gradient between these two sectors is 1.49 (the difference between area-mean AOD in a selected dust sector and that in a dust free sector). Thus, the indirect SW forcing of the Saharan dust from this case for nonraining clouds at solar zenith angle ~21.6° is 29.88 ± 2.42 (8.1%) W m^{-2} per unit AOD. The magnitude of indirect SW forcing for clouds with LWP of 100 g m^{-2} is about 56% of direct SW forcing of mineral dust in this case. To our knowledge, it is the first direct assessment of aerosol indirect forcing from measurements. The indirect SW forcing by mineral dust will have significant impacts on atmospheric dynamics.

The CERES resolution is coarser and the sample size is smaller than those of MODIS; we cannot study the radiation forcing at different cloud-top temperatures and different LWPs.

5. Conclusions

We show that clouds are affected strongly by the dust aerosols coming from the sub-Saharan region and that the effects do segregate and vary systematically when classified by cloud precipitation regime, cloud-top temperature, and LWP. We take these measures as surrogate estimators for cloud dynamics.

Nonprecipitating clouds with CTT in the range from 4° to 20°C show consistent behavior for all CTT subclasses, and the statistical significance improves with alternative subclassification by LWP. With classification by LWP the AIE = −0.07 to −0.17 (stronger with increasing LWP), with statistical significances ranging from 2.26σ to 5.47σ. The difference between the AIE for the first two LWP ranges is statistically significant; the observed AIE is weaker for the lowest LWP clouds and not distinctly different for the greater LWP ranges.

These are striking statistical significances, and the magnitude of the AIE is also larger than that found by Bréon et al. (2002) and Schwartz et al. (2002) for other aerosols. We can see that much of the improved statistical significance is due to the classification by cloud-top temperature and LWP. Even though we see evidence within the data that those retrievals are not error free, their statistical power demonstrates the importance of using these surrogate controls for cloud dynamics and that these retrievals are good enough to be helpful in the assessment of the Twomey effect.

Other satellite estimates of the aerosol indirect effect have shown large disparities in the magnitude of imputed affects, which have been extensively scrutinized by researchers (Rosenfeld and Feingold 2003; Shao and Liu 2005). We believe that by carefully segregating cloud precipitation regime and cloud-top height, the variability in estimated AIE may be reduced and the statistical significance improved for other aerosol types as well.

Studies of this kind require an estimate of the true degrees of freedom in the spatial data. We present a method for doing this and show that the results remain statistically significant, even for our classified subgroups, from these data. Had we not done this, the significances would appear much stronger.

The behavior of the raining clouds is different and we see AIE effects only for cloud-top temperatures less than 0°C. This itself is interesting and hard to explain with the classical Twomey effect. The results may be a consequence of precipitation efficiency or ice nucleus physics or vertical transport of mineral dust, but these attributions are speculative.

We also estimate radiation forcing of dust aerosols directly from satellite measurements. The direct shortwave (SW) radiation effect of Saharan dusts at solar zenith angle 21.6° is 53.48 ± 8.56 W m^{-2} per unit aerosol optical depth, with a correlation coefficient of 0.92. The indirect SW forcing of Saharan dust is 29.88 ± 2.42 W m^{-2} per unit AOD for clouds with LWP of 100 g m^{-2}. The indirect SW forcing of mineral dusts is about 56% of the direct dust SW forcing, which will have significant impacts on atmospheric dynamics. It should be emphasized here that, as a case study, results obtained here may not apply to other cases.

Acknowledgments. The authors thank Dr. Halstead Harrison for his valuable comments and assistance on analysis of degree of freedom. This research was supported by the Office of Science (BER), U.S. Department of Energy through the Atmospheric Radiation Measurement (ARM) Grant DE-FG02-03ER63531, and by the NOAA Educational Partnership Program with Minority Serving Institutions (EPP/MSI) under Cooperative Agreements NA17AE1625 and NA17AE1623. Dr. Li was also supported by National Natural Science Foundation of China (NSFC) Grants 40605010.

APPENDIX

Determination of Statistical Significance—Degrees of Freedom

The data are first treated as segregated classes by identified cloud-type category. We assume that this classification is phenomenological; near neighbors of different types are not correlated. Within each of these we then construct the conventional isotropic correlogram: the spatial correlation versus isotropic range. As it happens, the data here are close to the equator and not large in extent, so we use a simple range function in Euclidian degrees (great-circle distance corrections are negligible). One correlogram in r_e (LWP/τ) is shown in Fig. A1. These are Pearson correlation coefficients computed for the data pairs within a range bin as a function of range. Ripley (1981) discusses this standard definition of the correlogram and its use for problems of this kind.

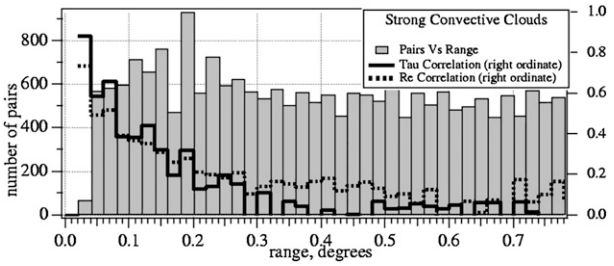

FIG. A1. Observed correlation vs range for strong convective rainy clouds.

The estimated degrees of freedom are then calculated four ways—all with the summation

$$D_f = \sum_{i=1}^{n} 1 \Big/ \left\{ 1 + \sum_{j=1}^{m} (1 - \delta_{i,j}) R[d(i, j)] \right\}. \quad \text{(A1)}$$

Here $d(i, j)$ is the distance between two points i and j and $R(d)$ is the Pearson correlation at that distance. This equation is itself an approximation justified for 1D Markovian correlations (i.e., a simple negative exponential for the correlogram). Papoulis and Unnikrishna Pillai (2002) discuss the 1D Markov problem. The four different uses of this are based on four different assumptions (note terms in bold appear in the tables).

(i) **Dfe** is computed using the binned empirical $R(d)$ of the correlogram. For this purpose $R(d)$ is set to zero for all ranges equal to and greater than the shortest-range with zero or negative correlation. The outer and inner summations are done only over the data in the CTT and LWP classification range, $n = m$. Arguably this is the most common assumption; the sum of **Dfe** for the subranges can be larger than the total over all ranges, and commonly is.

(ii) **Dfea** is computed identically to **Dfe** except that the inner summation is done over all the pixels of the classified cloud type—all cloud-top temperatures. This makes the conservative assumption that the clouds at different cloud-top temperatures are not really independent,

TABLE A1. Calculations of degree of freedom for all clouds segregated by cloud-top temperature.

T (°C)	N	Dfe	Dfea	Dff	Dffa
Nonrain clouds					
−20∼−10	1044	17.46	15.18	12.82	11.26
−10∼0	1091	17.93	12.01	13.24	9.10
0∼10	393	9.21	5.31	7.02	4.13
10∼20	3053	95.40	67.08	68.82	48.20
20∼30	2149	134.66	61.10	102.16	44.74
−20∼4	2144	30.22	27.44	22.55	20.56
4∼20	3437	97.57	72.14	70.64	52.12
Strong convective rainy clouds					
−20∼−10	52	6.79	5.60	6.59	5.29
−10∼0	73	6.48	5.61	5.86	5.00
0∼10	25	4.18	3.34	3.98	3.12
10∼20	282	45.91	36.21	42.45	33.00
20∼30	180	53.08	23.32	49.00	21.00
−20∼4	126	12.56	11.31	11.72	10.36
4∼20	306	47.73	39.45	44.12	36.05
Weak convective rainy clouds					
−20∼−10	60	5.07	4.11	4.29	3.65
−10∼0	66	4.57	3.27	4.11	2.93
0∼10	35	3.35	1.46	2.72	1.37
10∼20	207	17.46	14.69	14.82	12.32
20∼30	147	23.14	12.68	20.11	9.77
−20∼4	127	8.39	7.39	7.32	6.60
4∼20	241	19.38	16.12	16.19	13.66

for the purposes of this statistical experiment. Thus, m is the total of all pixels with this cloud type, and is larger than n for any CTT subrange. One consequence of this is that the sum of the **Dfea** for the CTT subranges is conservative and equal to the **Dfea** computed for all the data.

(iii) **Dff** is computed similarly to **Dfe** except that the $R(d) = e^{-d/x}$, where x is the best fit to the empirical correlogram over the range $d = 0$ to the first zero or negative binned correlation. Here **Dff** is an estimator congruent with the Markovian assumption underlying Eq. (A1); it is also generally more conservative than **Dfe**. To the extent that these measures are similar, we have better confidence that the estimation of the degrees of freedom is not unduly sensitive to assumptions and methodology.

(iv) **Dffa** is computed similarly to **Dff** except the inner summation is over all pixels.

The results computed with the two assumptions **e** and **f** are similar and well behaved (we expect estimate **f** to generally be less than estimate **e**) for all the data, which helps justify our use of Eq. (A1). The estimates **ea** and **fa** are smaller as expected, not uncommonly half that of the corresponding **e** and **f**. This is not very surprising, and it points out the central assumption made: that the classifications are ''independent data.'' The estimate **Dfe** is the most commonly used, and the resulting statistical significances are calculated with it. **Dfe** is the most optimistic of the four, but only slightly so compared to **Dff.** The four sets of estimated **Df** are listed in Tables A1 and A2 for various cloud regimes and stratifications.

TABLE A2. Calculations of degree of freedom for nonraining clouds segregated by cloud-top temperature and liquid water path.

LWP (g m^{-2})	N	Dfe	Dfea	Dff	Dffa
Temperature: −20° to 4°C					
75∼150	957	17.72	12.37	12.95	9.12
150∼225	490	12.47	5.87	9.25	4.45
225∼300	229	8.09	2.55	5.71	1.96
300∼375	23	1.56	0.41	0.95	0.31
Temperature: 4° to 20°C					
75∼150	941	73.22	15.69	54.47	11.77
150∼225	233	38.68	5.06	32.76	3.96
225∼300	75	17.78	1.53	14.78	1.20
300∼375	38	7.99	0.50	6.98	0.40

REFERENCES

Ackerman, A. S., and O. B. Toon, 2000: Effects of aerosols on cloud albedo: Evaluation of Twomey's parameterization of cloud susceptibility using measurements of ship tracks. *J. Atmos. Sci.,* **57,** 2684–2695.

Albrecht, B. A., 1989: Aerosols, cloud microphysics, and fractional cloudiness. *Science,* **245,** 1227–1230.

Berg, W., T. L'Ecuyer, and C. Kummerow, 2006: Rainfall climate regimes: The relationship of regional TRMM rainfall biases to the environment. *J. Appl. Meteor. Climatol.,* **45,** 434–454.

Bréon, F.-M., D. Tanré, and S. Generoso, 2002: Aerosol effect on cloud droplet size monitored from satellite. *Science,* **295,** 834–838.

Carlson, T. N., and J. M. Prospero, 1972: The large-scale movement of Saharan air outbreaks over the northern equatorial Atlantic. *J. Appl. Meteor.,* **11,** 283–297.

Christopher, S. A., and T. Jones, 2007: Satellite-based assessment of cloud-free net radiative effect of dust aerosols over the Atlantic Ocean. *Geophys. Res. Lett.,* **34,** L02810, doi:10.1029/2006GL027783.

Dunion, J. P., and C. S. Velden, 2004: The impact of the Saharan air layer on Atlantic tropical cyclone activity. *Bull. Amer. Meteor. Soc.,* **85,** 353–365.

Feingold, G., and Coauthors, 2003: First measurements of the Twomey indirect effect using ground-based remote sensors. *Geophys. Res. Lett.,* **30,** 1287, doi:10.1029/2002GL016633.

Gassó, S., and D. A. Hegg, 2003: On the retrieval of columnar aerosol mass and CCN concentration by MODIS. *J. Geophys. Res.,* **108,** 4010, doi:10.1029/2002JD002382.

Geier, E., R. Green, D. Kratz, P. Minnis, W. Miller, S. Nolan, and C. Franklin, 2003: Clouds and the Earth's Radiant Energy System (CERES) data management system: Single satellite footprint TOA/surface fluxes and clouds (SSF) collection document. Release 2, version 1, NASA Langley Research Center, 235 pp. [Available online at http://asd-www.larc.nasa.gov/ceres/collect_guide/SSF_CG.pdf.]

Han, Q., W. B. Rossow, J. Chou, and R. M. Welch, 1998: Global survey of the relationships of cloud albedo and liquid water path with droplet size using ISCCP. *J. Climate,* **11,** 1516–1528.

Houze, R. A., 1997: Stratiform precipitation in regions of convection: A meteorological paradox? *Bull. Amer. Meteor. Soc.,* **78,** 2179–2195.

Kapustin, V. N., A. D. Clarke, Y. Shinozuka, S. Howell, V. Brekhovskikh, T. Nakajima, and A. Higurashi, 2006: On the determination of a cloud condensation nuclei from satellite: Challenges and possibilities. *J. Geophys. Res.,* **111,** D04202, doi:10.1029/2004JD005527.

Kaufman, Y. J., I. Koren, L. A. Remer, D. Tanré, P. Ginoux, and S. Fan, 2005: Dust transport and deposition observed from the *Terra*-Moderate Resolution Imaging Spectroradiometer (MODIS) spacecraft over the Atlantic Ocean. *J. Geophys. Res.,* **110,** D10S12, doi:10.1029/2003JD004436.

Kim, B.-G., S. E. Schwartz, M. A. Miller, and Q. Min, 2003: Effective radius of cloud droplets by ground-based remote sensing: Relationship to aerosol. *J. Geophys. Res.,* **108,** 4740, doi:10.1029/2003JD003721.

King, M. D., S.-C. Tsay, S. E. Platnick, M. Wang, and K.-N. Liou, 1997: Cloud retrieval algorithms for MODIS: Optical thickness, effective particle radius, and thermodynamic phase. MODIS Algorithm Theoretical Basis Document ATBD-MOD-05, 79 pp. [Available online at http://modis.gsfc.nasa.gov/data/atbd/atbd_mod05.pdf.]

Kummerow, C., and Coauthors, 2001: The evolution of the Goddard profiling algorithm (GPROF) for rainfall estimation from passive microwave sensors. *J. Appl. Meteor.,* **40,** 1801–1820.

Liu, X., J. Wang, and S. A. Christopher, 2003: Shortwave direct radiative forcing of Saharan dust aerosols over the Atlantic Ocean. *Int. J. Remote Sens.,* **24,** 5147–5160.

Min, Q.-L., R. Li, B. Lin, E. Joseph, S. Wang, Y. Hu, V. Morris, and F. Chang, 2009: Evidence of mineral dust altering cloud microphysics and precipitation. *Atmos. Chem. Phys.,* **9,** 3223–3231.

Morris, V., and Coauthors, 2006: Measuring trans-Atlantic aerosol transport from Africa. *Eos, Trans. Amer. Geophys. Union,* **87,** doi:10.1029/2006EO500001.

Nalli, N. R., and Coauthors, 2005: Profile observations of the Saharan air layer during AEROSE 2004. *Geophys. Res. Lett.,* **32,** L05815, doi:10.1029/2004GL022028.

——, and Coauthors, 2006: Ship-based measurements for infrared sensor validation during the Aerosol and Ocean Science Expedition 2004. *J. Geophys. Res.,* **111,** D09S04, doi:10.1029/2005JD006385.

Olson, W. S., Y. Hong, C. Kummerow, and J. Turk, 2001: A texture-polarization method for estimating convective–stratiform precipitation area coverage from passive microwave radiometer data. *J. Appl. Meteor.,* **40,** 1577–1591.

——, and Coauthors, 2006: Precipitation and latent heating distributions from satellite passive microwave radiometry. Part I: Improved method and uncertainties. *J. Appl. Meteor. Climatol.,* **45,** 702–720.

Papoulis, A., and S. Unnikrishna Pillai, 2002: *Probability, Random Variables, and Stochastic Processes*. 4th ed. McGraw-Hill, 852 pp.

Ramanathan, V., and Coauthors, 2001: Indian Ocean Experiment: An integrated analysis of the climate forcing and effects of the great Indo-Asian haze. *J. Geophys. Res.,* **106** (D22), 28 371–28 398.

Ripley, D. B., 1981: *Spatial Statistics*. John Wiley & Sons, 252 pp.

Rosenfeld, D., and G. Feingold, 2003: Explanation of the discrepancies among satellite observations of the aerosol indirect effect. *Geophys. Res. Lett.,* **30,** 1776, doi:10.1029/2003GL017684.

Sassen, K., 2002: Indirect climate forcing over the western U.S. from Asian dust storms. *Geophys. Res. Lett.,* **29,** 1465, doi:10.1029/2001GL014051.

Schwartz, S. E., Harshvardhan, and C. M. Benkovitz, 2002: Influence of anthropogenic aerosol on cloud optical depth and albedo shown by satellite measurements and chemical transport modeling. *Proc. Natl. Acad. Sci. USA,* **99,** 1784–1789.

Shao, H., and G. Liu, 2005: Why is the satellite observed aerosol's indirect effect so variable? *Geophys. Res. Lett.,* **32,** L15802, doi:10.1029/2005GL023260.

Toon, O. B., 2003: African dust in Florida clouds. *Nature,* **424,** 623–624.

Twomey, S., 1974: Pollution and the planetary albedo. *Atmos. Environ.,* **8,** 1251–1256.

——, 1977a: The influence of pollution on the shortwave albedo of clouds. *J. Atmos. Sci.,* **34,** 1149–1152.

——, 1977b: *Atmospheric Aerosols*. Elsevier, 302 pp.

Wielicki, B. A., B. R. Barkstrom, E. F. Harrison, R. B. Lee, G. L. Smith, and J. E. Cooper, 1996: Clouds and the Earth's Radiant Energy System (CERES): An Earth observing system experiment. *Bull. Amer. Meteor. Soc.,* **77,** 853–868.

Wilheit, T., C. D. Kummerow, and R. Ferraro, 2003: Rainfall algorithms for AMSR-E. *IEEE Trans. Geosci. Remote Sens.,* **41,** 204–214.